



# Tropical forcing of Australian extreme low minimum temperatures in September 2019

Eun-Pa Lim<sup>1</sup> · Harry H. Hendon<sup>1</sup> · Li Shi<sup>1</sup> · Catherine de Burgh-Day<sup>1</sup> · Debra Hudson<sup>1</sup> · Andrew King<sup>2</sup> ·  
Blair Trewin<sup>1</sup> · Morwenna Griffiths<sup>1</sup> · Andrew Marshall<sup>1</sup>

Received: 13 July 2020 / Accepted: 17 January 2021 / Published online: 20 February 2021  
© Crown 2021

## Abstract

We explore the causes and predictability of extreme low minimum temperatures ( $T_{\min}$ ) that occurred across northern and eastern Australia in September 2019. Historically, reduced  $T_{\min}$  is related to the occurrence of a positive Indian Ocean Dipole (IOD) and central Pacific El Niño. Positive IOD events tend to locate an anomalous anticyclone over the Great Australian Bight, therefore inducing cold advection across eastern Australia. Positive IOD and central Pacific El Niño also reduce cloud cover over northern and eastern Australia, thus enhancing radiative cooling at night-time. During September 2019, the IOD and central Pacific El Niño were strongly positive, and so the observed  $T_{\min}$  anomalies are well reconstructed based on their historical relationships with the IOD and central Pacific El Niño. This implies that September 2019  $T_{\min}$  anomalies should have been predictable at least 1–2 months in advance. However, even at zero lead time the Bureau of Meteorology ACCESS-S1 seasonal prediction model failed to predict the anomalous anticyclone in the Bight and the cold anomalies in the east. Analysis of hindcasts for 1990–2012 indicates that the model's teleconnections from the IOD are systematically weaker than the observed, which likely stems from mean state biases in sea surface temperature and rainfall in the tropical Indian and western Pacific Oceans. Together with this weak IOD teleconnection, forecasts for earlier-than-observed onset of the negative Southern Annular Mode following the strong polar stratospheric warming that occurred in late August 2019 may have contributed to the  $T_{\min}$  forecast bust over Australia for September 2019.

**Keywords** Extremes · Predictability · Teleconnections

## 1 Introduction

Climate anomalies during 2019 were extraordinary across the globe with the concurrence of a central Pacific El Niño<sup>1</sup> (also referred to as El Niño Modoki or warm-pool El Niño) event (Ashok et al. 2007; Kao and Yu 2009; Kug et al. 2009), a near-record strength positive Indian Ocean Dipole mode event (IOD; Saji et al. 1999), and a record-strong weakening and warming of the Southern Hemisphere stratospheric polar vortex and subsequent development of record-strong negative phase of the Southern Annular Mode event (SAM; Thompson and Wallace 2000) during September–December (Lim et al. 2020). All

these phenomena are well-known drivers of hot and dry conditions over Australia especially during austral spring and summer (Saji et al. 2005; Hendon et al. 2007; Wang and Hendon 2007; Ummenhofer et al. 2009; Risbey et al. 2009; Marshall et al. 2014; Lim and Hendon 2015; Lim et al. 2019). Indeed, the Australian monthly mean maximum temperature was in the top decile category and monthly mean rainfall was in the bottom decile category during September to December 2019 based on 110- and 120-year observational records, respectively.<sup>2</sup> Austral spring (September to November) and the individual months of November and December 2019 were also the driest on record.

In stark contrast to the significantly higher-than-normal monthly mean (hereafter, referred to as monthly) maximum

✉ Harry H. Hendon  
harry.hendon@bom.gov.au

<sup>1</sup> Bureau of Meteorology, Melbourne, VIC, Australia

<sup>2</sup> School of Earth Sciences, ARC Centre of Excellence for Climate Extremes, University of Melbourne, Parkville, VIC, Australia

<sup>1</sup> The term "central Pacific El Niño" is used in this study to describe an event whose maximum SST anomaly is found near the dateline. This will not necessarily correspond to a canonical El Niño whose maximum SST anomaly is found across the equatorial central to eastern Pacific.

<sup>2</sup> <http://www.bom.gov.au/climate/change/#tabs=Tracker&track=timeseries>.

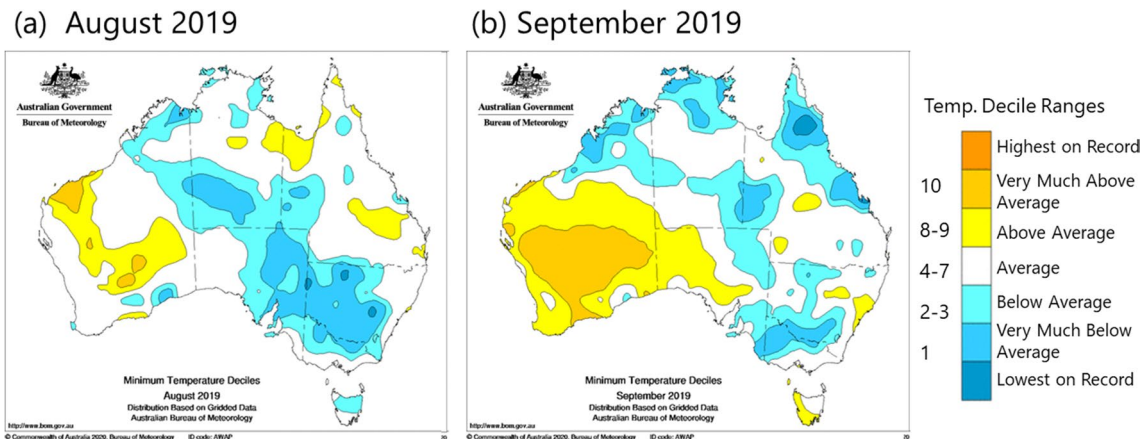


**Fig. 1** Deciles of monthly mean of daily minimum temperatures for **a** August and **b** September 2019. Deciles are computed based on 1910–2019. Data are from <http://www.bom.gov.au/jsp/awap/temp/index.jsp>

temperatures, monthly mean minimum temperatures were significantly lower than normal in many locations over Australia during August and September 2019 (Fig. 1). Frost events in September led to severe crop damage (<http://www.bom.gov.au/climate/current/month/aus/archive/201909.summary.shtml>), which was exacerbated by low rainfall and high day-time temperatures during September and the months that followed.

Anomalously low minimum temperatures can have a significant impact on a wide range of primary industries, affecting productivity of beef and dairy cattle (Webster et al. 2008; Cowan et al. 2019), cotton (Bange and Milroy 2004), rice (Jacobs and Pearson 1999; Hatfield and Prueger 2015), sugarcane (Grantz 1989), and viticulture (Keller et al. 2010). Especially, severe frosts are a major risk for agriculture in Australia (Frederiks et al. 2015; Zheng et al. 2015). For instance, widespread and protracted frost events in early spring can have a deleterious impact on wheat and horticultural plants that flower prior to early October (Rebeck et al. 2007; Pook et al. 2009). Frost damage can cost the Australian grains industry about \$360 million Australian dollars per year (Risbey et al. 2019). A common strategy to minimize the risk of frost damage is to delay planting to avoid the most frost-sensitive stages of crop development occurring during the high frost risk period from mid-August to late September. Frost damage also affects the timing of cutting crops to make hay.

Despite such substantial impacts of low minimum temperatures on the productivity of primary industries, relatively little attention has been paid to understanding the causes and long range predictability of low minimum temperatures over Australia as compared to maximum temperatures and rainfall, although there has been a growing volume of research regarding frosts (Dittus et al. 2014; Crimp et al. 2016; Grose et al. 2018; Risbey et al. 2019). Therefore,

here we have attempted to improve our understanding of the variability and predictability of low minimum temperatures over Australia by examining the cold extreme case of September 2019, for which many regions of northern and eastern Australia experienced September-mean minimum temperature ( $T_{\min}$ ) in the bottom two deciles. Because cold extremes potentially have a significant impact on agriculture in early spring by influencing the critical stages of plant life cycle, including the timing of head emergence and flowering of winter crops (Crimp et al. 2016), we have focused on the anomalously low  $T_{\min}$  of September 2019 although south-eastern Australia also experienced extreme low  $T_{\min}$  in August 2019 (Fig. 1).

In this study, we first investigate what caused the widespread low minimum temperatures during September 2019, which is especially intriguing given the enormous interest in the hot and dry conditions that occurred later in austral spring 2019 across eastern Australia and the subsequent spate of devastating bushfires (<http://www.bom.gov.au/climate/current/statements/scs72.pdf>) (Boer et al. 2020). We also assess the predictability of the occurrence of extreme  $T_{\min}$  during September 2019 using historical relationships with known drivers of low minimum temperatures and with the Australian Bureau of Meteorology (BoM)'s dynamical sub-seasonal to seasonal climate forecast system ACCESS-S1 (the Australian Community Climate and Earth System Simulator-Seasonal prediction system version 1; Hudson et al. 2017) with an aim to elucidate areas for improvement in the future development of the forecast system.

## 1.1 Data and forecast system

For the observational analysis of Australian  $T_{\min}$ , we used the Australian Water Availability Project (AWAP) monthly mean gridded analyses of daily  $T_{\min}$ , which are provided on

a 5 km grid (Jones et al. 2009).  $T_{\min}$  is indicative of the 2-m air temperature as measured, for instance, in a meteorological screen. Three extreme indices (adapted from Zhang et al. 2011) were also calculated at each grid point using the daily AWAP  $T_{\min}$  analyses: the coldest minimum temperature of the month, and the number of days with daily minimum temperatures below 2 °C and 0 °C. Frost occurs when the ground temperature drops to freezing (or below). Frost can occur when the 2-m air temperature is as warm as 2 °C as a result of a near surface inversion due to enhanced surface radiative cooling (also known as ground frost; <https://www.metoffice.gov.uk/weather/learn-about/weather/types-of-weather/frost-and-ice/frost>) (Kalma et al. 1992). A hard frost (or freeze) is assumed to have occurred when the 2-m temperature drops to 0 °C (or below) (also known as air frost; <https://www.metoffice.gov.uk/weather/learn-about/weather/types-of-weather/frost-and-ice/frost>). We investigate atmospheric circulation anomalies using the analyses of mean sea level pressure (MSLP), 10-m zonal (U) and meridional (V) winds and total cloud cover fraction from the Japanese 55-year ReAnalysis (JRA-55), which are provided daily on a ~55 km horizontal grid (Kobayashi et al. 2015). For sea surface temperature (SST), we use the Hurrell et al. (2008) monthly mean analyses, which is based on the HadISST analyses (Rayner et al. 2003) up to 1981, and the Reynolds et al. (2002) optimum interpolation (OI) version 2 SST analyses for 1982–2019.

Anomalies of all the observational variables were computed relative to the climatological mean over 1990–2012, which is the period when the ACCESS-S1 hindcasts are available. Correlation and regression analyses using the observational data were conducted for 1979–2018. It is worth noting here that the AWAP  $T_{\min}$  analysis shows few areas of strong trends in September during the period 1979–2018 except in the far south of Queensland, where there is a warming trend, and in some locations of Western Australia and southern Australia, where there is a cooling trend<sup>3</sup> (statistically significant at the 10% level, assessed by a two-tailed Student's t test; Supplementary Fig S1).

Forecasts of Australian  $T_{\min}$  and associated large-scale circulations were produced from ACCESS-S1 (Hudson et al. 2017). This system, which is based on the UKMO GloSea5 system (MacLachlan et al. 2015), is a state-of-the-art dynamical sub-seasonal to seasonal climate forecast system, which became operational at BoM in August 2018. The atmosphere is resolved on a ~60 km grid with 85 vertical levels, fully resolving the stratosphere. The ocean is resolved

at 25 km with 75 vertical levels. The atmosphere, land and ocean component models are coupled every three hours.

11-member hindcasts of ACCESS-S1 out to 6-month lead time are available for 1990–2012 at four different initialisation dates per month (1st, 9th, 17th and 25th). The model atmosphere (zonal and meridional winds, temperatures, humidity and surface pressure) and soil temperatures were initialised using the European Centre for Medium-Range Forecasts Interim Reanalysis (ERA-Interim) data (Dee et al. 2011), while the model soil moisture was initialised with the climatology of ERA-Interim (over 1990–2012) (MacLachlan et al. 2015). The ocean was initialised with the analysis from the Met Office Forecast Ocean Assimilation Model (FOAM; Waters et al. 2015).

The 11-member ensemble was produced by perturbing the atmospheric initial conditions only (Hudson et al. 2017). For this study, we have formed a 22 member ensemble by utilising the forecasts initialised on the 1st of a month and the 25th of the previous month. For instance, the lead time 0 forecasts for September consists of the 11-member ensemble forecasts initialised on the 1st of September and the 11-member ensemble forecasts initialised on the 25th of August.

The real-time forecasts using the operational system for September 2019 were initialised with the atmospheric conditions from BoM's numerical weather prediction system (similar atmospheric model to ACCESS-S1 but with higher horizontal resolution) and the ocean conditions provided from FOAM. The real-time system produces an 11-member ensemble of forecasts everyday. Generation of forecast products provided by the BoM Climate Service uses a lagged ensemble approach to form a 99-member ensemble (9 consecutive days for the seasonal forecast products). For this study, we formed a 22-member ensemble by combining the eleven members from the real-time forecasts initialised on the 1st of a month and on the 25th of the previous month to be consistent with our hindcast analysis. Further details of the ACCESS-S1 model configuration, initialisation, ensemble generation and forecast performance can be found in Hudson et al. (2017).

## 2 Results

### 2.1 Cold extremes in September 2019

The monthly  $T_{\min}$  for September 2019 was anomalously low over northern and eastern Australia, which contrasted to the higher-than-normal  $T_{\min}$  over the southern half of Western Australia (Fig. 2). Some parts of northern and eastern Australia experienced  $T_{\min}$  in the bottom 20% (i.e., bottom quintile) based on 110-year data (Fig. 1b). If we consider the most recent 40 years,  $T_{\min}$  anomalies in

<sup>3</sup> This could be partly influenced by a cool bias in recent AWAP  $T_{\min}$  data, relative to the homogenised ACORN-SAT dataset, driven in part by the movement of sites from town to out-of-town locations in the 1990s and 2000s (Trewin 2018; Trewin et al. 2020).

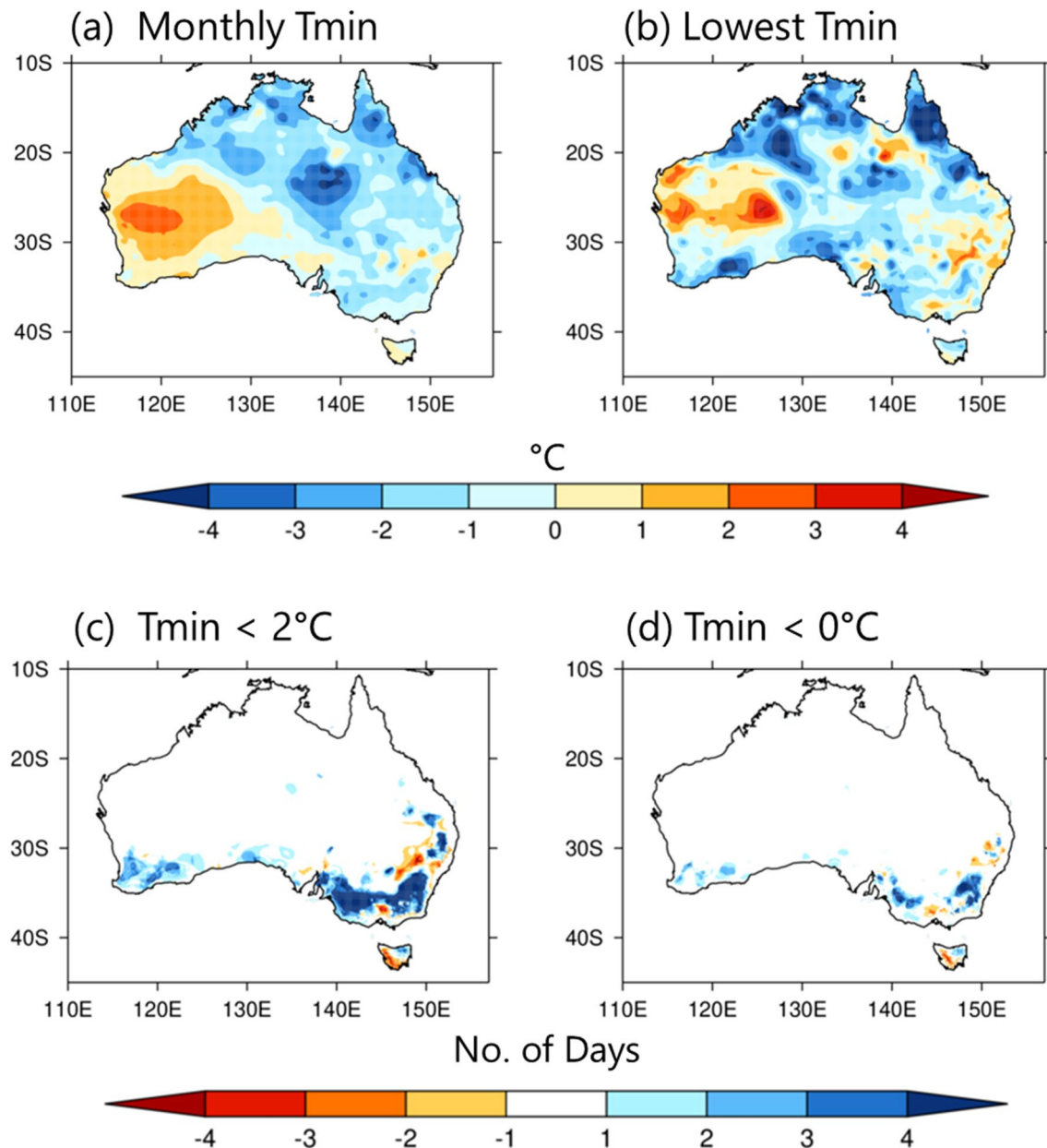


**Fig. 2** September 2019 anomalies of **a** monthly mean  $T_{\text{min}}$ , **b** lowest  $T_{\text{min}}$ , **c** number of days when  $T_{\text{min}}$  is below  $2^{\circ}\text{C}$  and **d** number of days when  $T_{\text{min}}$  is below  $0^{\circ}\text{C}$  compared to their respective climatolo-

gies over the period 1990–2012. Note that in **c** and **d** the increased number of days with  $T_{\text{min}}$  below  $2^{\circ}\text{C}$  and  $0^{\circ}\text{C}$  is shown with the blue colour shading

September 2019 are in the extreme cold categories (bottom 20%) over larger areas in the north and the east, while the anomalies of opposite sign in southern Western Australia are in the top 10% (i.e., top decile) (Supplementary Fig. S2).

The lowest minimum temperatures in September 2019 were up to  $4^{\circ}\text{C}$  lower than the climatology of 1990–2012 over the northern parts of Northern Territory and Western Australia and the northeast of Queensland (Fig. 2b). Moreover, the southernmost part of the Australian continent,

especially over eastern South Australia, northern Victoria and parts of southern inland New South Wales, experienced an above-average number of days with  $T_{\text{min}}$  below  $2^{\circ}\text{C}$ , a common threshold for potential frost formation (e.g., Kalma et al. 1992), and some areas even had an above-average number of days of hard frost with  $T_{\text{min}}$  below  $0^{\circ}\text{C}$  (Fig. 2c, d). The increased number of days with  $T_{\text{min}}$  below  $0^{\circ}\text{C}$  is concentrated over the Great Dividing Range in the southeast of the continent and reflects an orographic lowering of  $T_{\text{min}}$  values. The pattern of enhanced occurrence of days

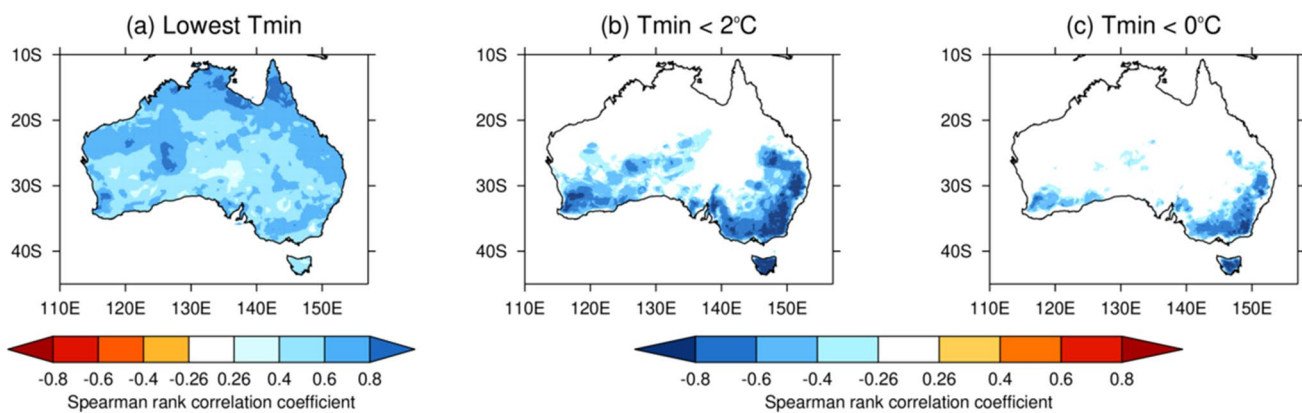


**Fig. 3** Spearman rank correlation of monthly  $T_{\text{min}}$  with **a** lowest  $T_{\text{min}}$ , **b** number of days when  $T_{\text{min}} < 2^{\circ}\text{C}$  and **c** number of days when  $T_{\text{min}} < 0^{\circ}\text{C}$  in September. Note that red shading indicates negative correlation and blue indicates positive correlation in **(a)**, displaying lower monthly  $T_{\text{min}}$  positively correlated with lower lowest  $T_{\text{min}}$ , whereas red shading indicates positive correlation and blue shading indicates negative correlation in **b** and **c**, displaying

monthly  $T_{\text{min}}$  negatively correlated with the number of extreme cold nights (i.e. lower monthly  $T_{\text{min}}$  is associated with increased number of days with  $T_{\text{min}} < 2^{\circ}\text{C}$  and  $< 0^{\circ}\text{C}$  in **b** and **c**, respectively). Spearman rank correlation is used because the extreme threshold-based indices are non-Gaussian and therefore require analysis using non-parametric methods

with September  $T_{\text{min}} < 0^{\circ}\text{C}$  and  $2^{\circ}\text{C}$  in the southeast of the country is typical of what occurs during this month when the local monthly  $T_{\text{min}}$  is below normal (Fig. 3).<sup>4</sup>

## 2.2 Drivers of cold nights over northern and eastern Australia

To investigate what drives the interannual variability of September minimum temperature of Australia, with the ultimate goal to understand what caused the 2019 September  $T_{\text{min}}$  anomaly, we first explore the link to tropical SST variations. We do this by reconstructing 2019 September SST anomalies with the following steps: first, we regress gridded SSTs on the inversely signed eastern Australian areal-mean  $T_{\text{min}}$  (averaged over land points east of  $140^{\circ}\text{E}$  and north of  $45^{\circ}\text{S}$ ; EAU  $T_{\text{min}}$ ) for September using data for 1979–2018 (Fig. 4b). Here the inverse  $T_{\text{min}}$  was used to highlight the SST pattern associated with lower-than-normal minimum temperatures. Although there is no significant linear trend detected in the eastern Australia areal-mean  $T_{\text{min}}$  of September (likely because of the offset between the cooling trend in the southeast and the warming trend in the northeast of the country), we de-trend the EAU  $T_{\text{min}}$  time series. Second, we scale the resultant regression coefficients at each grid point by the magnitude of the inverse  $T_{\text{min}}$  of September 2019,

and therefore, the SST anomalies expected from the statistical relationship with September EAU  $T_{\text{min}}$  and for the 2019 EAU  $T_{\text{min}}$  anomaly are obtained.

The reconstructed SST pattern displayed in Fig. 4a bears a signature of the positive phase of the Indian Ocean Dipole (IOD), which is characterised by colder-than-normal sea surface in the tropical eastern Indian Ocean ( $0\text{--}10^{\circ}\text{S}, 90\text{--}110^{\circ}\text{E}$ ) and concurrent warmer-than-normal sea surface in the tropical western Indian Ocean ( $10^{\circ}\text{S}\text{--}10^{\circ}\text{N}, 50\text{--}70^{\circ}\text{E}$ ; Saji et al. 1999). Although eastern Australian  $T_{\text{min}}$  is more correlated with the SSTs in the eastern pole of the IOD during September, the SSTs in the eastern pole of the IOD is correlated with the index of the IOD, the Dipole Mode Index (DMI), at 0.9 in this month. Thus, we can subsequently quantify the relationship of  $T_{\text{min}}$  with the tropical Indian Ocean SST variations using the DMI. Eastern Australian  $T_{\text{min}}$  is also seen to be significantly related to the occurrence of central Pacific (CP) El Niño, which is characterised by warmer-than-normal sea surface in the vicinity of the equatorial dateline ( $10^{\circ}\text{S}\text{--}10^{\circ}\text{N}, 165\text{--}220^{\circ}\text{E}$ ) flanked by colder-than-normal SSTs in the far east ( $15^{\circ}\text{S}\text{--}5^{\circ}\text{N}, 250\text{--}290^{\circ}\text{E}$ ) and west ( $10^{\circ}\text{S}\text{--}20^{\circ}\text{N}, 125\text{--}145^{\circ}\text{E}$ ; Ashok et al. 2007).

The observed SST anomaly in September 2019 (Fig. 4b) shows a pattern of both positive IOD and CP El Niño, which is quantified by positive amplitudes greater than one standard deviation ( $\sigma$ ) of the DMI from May 2019 until January 2020; and the El Niño Modoki Index (EMI; Ashok et al. 2007) from April to October 2019 (Supplementary Fig. S3). In September 2019, the DMI was  $+1.6\sigma$ , which is the 2nd highest September value after 1994. There is a weak positive trend found in the September DMI derived

<sup>4</sup> Here we have used the Spearman rank correlation to relate the occurrences of days with  $T_{\text{min}} < 2$  and  $0^{\circ}\text{C}$  to the monthly  $T_{\text{min}}$  at each gridpoint because the relationship may not be linear although we assume the relationship between monthly  $T_{\text{min}}$  and number of days below a threshold is monotonic (i.e., number of days below 2 and  $0^{\circ}\text{C}$  increases with lower values of monthly mean  $T_{\text{min}}$ ).

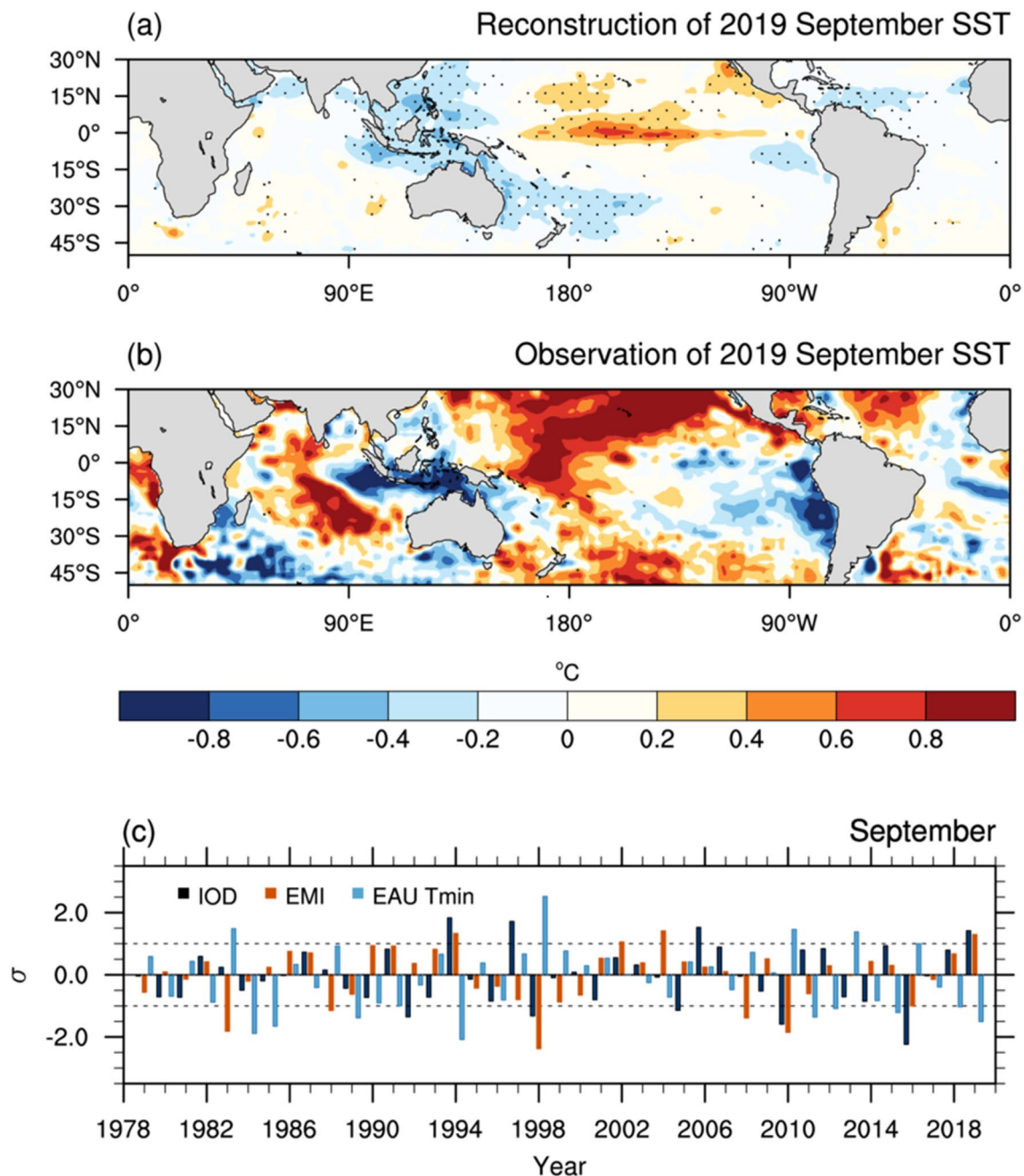


**Fig. 4** **a** Reconstruction of 2019 September SST anomalies using regression of SSTs on the inversely signed de-trended eastern Australian  $T_{\min}$  averaged over land points of  $140\text{--}156^{\circ}\text{E}$ ,  $45\text{--}10^{\circ}\text{S}$  (shown in **c**) for September 1979–2018, **b** SST anomalies for September 2019, and **c** time series of the de-trended Indian Ocean Dipole mode index (DMI; dark blue bars), the de-trended El Niño Modoki

Index (EMI; orange bars), and the de-trended areal-mean eastern Australian  $T_{\min}$  of September (EAU  $T_{\min}$ ; light blue bars). In **a** reconstruction was obtained by scaling the regression coefficients by the magnitude of EAU  $T_{\min}$  in 2019. Stippling in **b** indicates the statistical significance of the regression coefficients at the 10% level

from the SST data used in this study but is not statistically significant at the 10% level as assessed by a two-tailed Student-t test with 39 degrees of freedom (i.e., 40 samples

of 1979–2018 minus 1). Nonetheless, de-trending alters the ranking of the 2019 IOD event to be the 4th highest on the same 40 year record (the de-trended DMI being  $+1.4\sigma$

(Fig. 4c).<sup>5</sup> The EMI was  $+1.2\sigma$ , the 3rd highest on record for the month with and without a 40-year linear trend (i.e., no trend in the time series) (Fig. 4c). EAU  $T_{\min}$  for September 2019 was the 4th coldest in the same period (Fig. 4c). The lowest minimum temperature over eastern Australia for September occurred in 1994, with slightly larger DMI and EMI values than 2019.

Over the period 1979–2018, the correlation of EAU  $T_{\min}$  with the DMI and with the EMI (with or without considering the 40-year trend) during September is  $-0.4$  and  $-0.6$ , respectively. Spatially, the significant correlation of monthly  $T_{\min}$  during September with the DMI is concentrated in the southeast along the Dividing Range and in the far northwest (Fig. 5a), whereas the significant correlation with the EMI is mainly in the central north and east (Fig. 5b). The high correlation of the DMI with the number of days with  $T_{\min} < 2$  and  $0^{\circ}\text{C}$  is similarly localised in the southeast along the Dividing Range (Fig. 5c, e), whereas the high correlation with the EMI is concentrated in the eastern Murray-Darling Basin (Fig. 5d, f). Similar correlation patterns of the monthly  $T_{\min}$  are found between the lowest  $T_{\min}$  and the DMI and the EMI (Fig. 5g, h).

Based on these relationships in Fig. 5, we can reconstruct (or synthesize)  $T_{\min}$  anomalies using multiple linear regression with the de-trended DMI and EMI as predictors.<sup>6</sup> The explained variance of monthly  $T_{\min}$  for September using this regression model is displayed in Fig. 6a (expressed as the correlation of reconstructed  $T_{\min}$  with observed  $T_{\min}$  over the period 1979–2018). The explained variance ranges up to 60% along the east coast and extending across the far north. This regression model then can be used to successfully reconstruct the September 2019 observed anomalies (Fig. 6b) by plugging in the observed values of the de-trended DMI and EMI for September 2019 (Fig. 6c). The pattern correlation between the observed and the reconstructed  $T_{\min}$  anomalies for 2019 (i.e., between Fig. 6b and c) is 0.8.

<sup>5</sup> The DMI derived from the HadISST data set (available at Climate Explorer) shows a strong positive trend since the 1960s, and consequently, the 2019 DMI was the highest on record since 1979 before removing the linear trend and the 2nd highest after removing the trend. For the consistency of the SST data for the DMI and the EMI, we computed our own DMI and EMI using the SST data described in Sect. 2. While the positive trend in the DMI is significantly stronger in the HadISST than in the data used in this study, the de-trended DMI of the HadISST is highly correlated with our de-trended DMI by 0.9.

<sup>6</sup> The de-trended DMI and EMI are correlated by 0.3 in September, which is statistically significant at the 10% level, as assessed by a two-tailed Student-t test with 40 samples of 1979–2018. This moderate collinearity of the two indices is appropriately dealt with in multiple linear regression calculation. See Supplementary Information for the calculations of the total explained variance and regression coefficients.

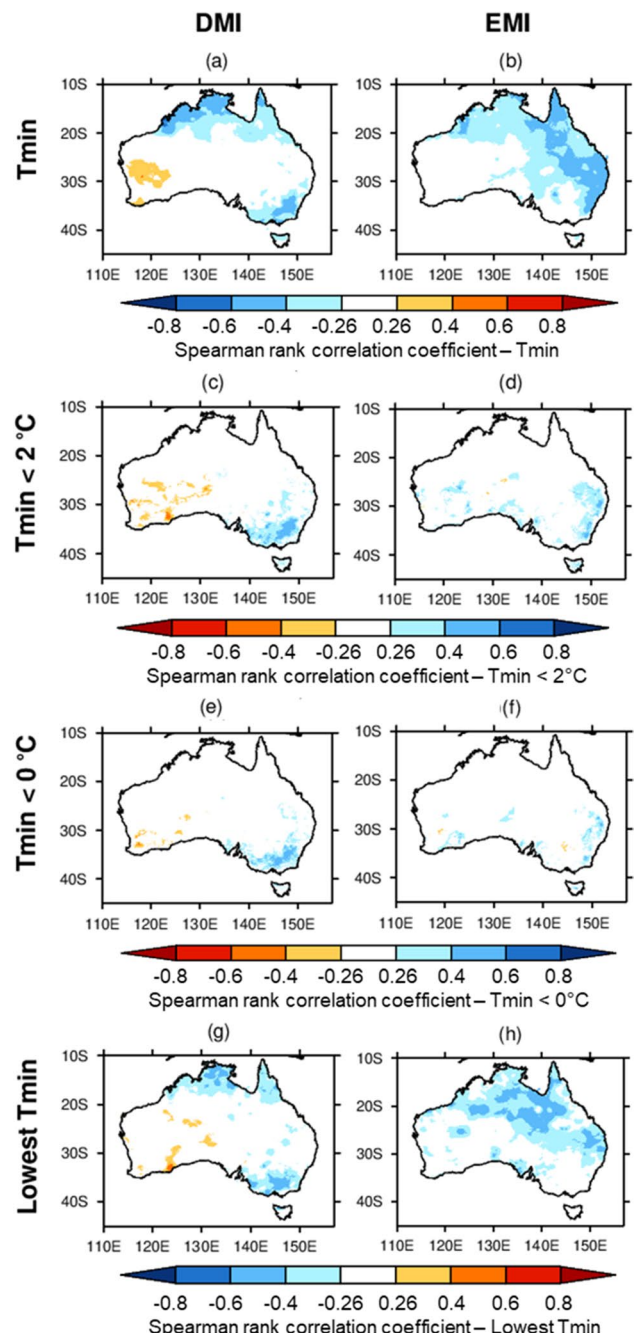


**Fig. 5** Spearman's rank correlation of **a, b** September-mean  $T_{\min}$ , **c, d** number of days in September with  $T_{\min} < 2^{\circ}\text{C}$ , **e, f** number of days in September with  $T_{\min} < 0^{\circ}\text{C}$ , and **g, h** lowest  $T_{\min}$  during September with the de-trended DMI (left) and the de-trended EMI (right). Positive correlation is shown with blue colour shading in **c–f** to indicate positive DMI and EMI are associated with increased days for  $T_{\min} < 2^{\circ}\text{C}$  and  $< 0^{\circ}\text{C}$

In order to gain more insight into the causes of the widespread low  $T_{\min}$  for September 2019, we display in the left column of Fig. 7 the anomalies of MSLP, 10-m horizontal winds and total cloud cover fraction for September 2019. To

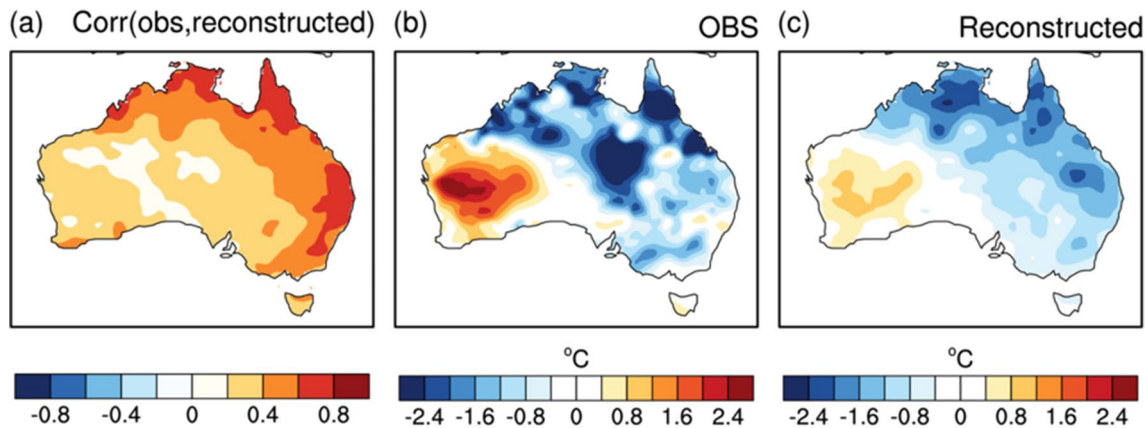


**Fig. 6** **a** Pearson correlation between the observed  $T_{\min}$  and the reconstruction of  $T_{\min}$  using the de-trended DMI and the de-trended EMI over 1979–2018, **b** observed  $T_{\min}$  anomalies for September 2019 (same as Fig. 2a), and **c** reconstruction of  $T_{\min}$  anomalies for September 2019 using the same multiple linear regression model as in (a).

The pattern correlation between **b** and **c** is 0.8. The reconstruction of  $T_{\min}$  was obtained by regressing  $T_{\min}$  anomalies onto the de-trended DMI and EMI over 1979–2018 and multiplying the resultant regression coefficients by the de-trended DMI and EMI time series

assist comparison, we display the observed September 2019  $T_{\min}$  anomaly map (Fig. 2a) here again (Fig. 7e). The middle and right columns of Fig. 7 display the composite anomalies during the five strongest positive IOD events and the five strongest CP El Niño events observed during 1979–2018 (years are listed in Table 1), respectively. The observed 2019 circulation anomalies are characterised by a strong high pressure anomaly centered over the Great Australian Bight and associated significant northward winds advecting cold air from the south and westward winds blowing towards Western Australia. Also, there is a 4–10% reduction in the total cloud cover fraction over northern and eastern Australia, which would have increased outgoing longwave radiation (i.e., radiative cooling to space), therefore promoting enhanced night-time cooling. These circulation and cloud fraction anomalies are similar to what typically occurs during positive IOD years (middle column of Fig. 7) and, to a lesser degree, during the strong CP El Niño years (right column Fig. 7). The analysis presented in Fig. 7 confirms the important role of the IOD and central Pacific El Niño for promoting the low  $T_{\min}$  anomalies observed during September 2019.

We have also examined the composite anomalies for strong negative IOD years and strong CP La Niña years and found that the circulation anomalies are not symmetrically opposite to their positive counterparts over the midlatitudes (Supplementary Fig. S4), and the pressure anomalies and related horizontal wind anomalies are mostly not statistically significant at the 10% level. On the other hand, negative IOD and CP La Niña are related to significant low pressure anomalies in the tropical eastern Indian Ocean and over the Maritime Continent and significant increases of total cloud cover over eastern Australia (Supplementary Fig S4). These

anomalous conditions appear to be closely tied to higher  $T_{\min}$  over the north and the subtropical east of the country observed during the negative IOD and CP La Niña years.

### 2.3 ACCESS-S1 forecasts

IOD events generally start to develop during austral winter, peak in late spring and then typically decay in December when the Australian summer monsoon commences (Saji et al. 1999; Zhao and Hendon 2009; Hendon et al. 2012). The skill for predicting the IOD, as expressed by temporal correlation of the DMI indices between the observation and the prediction based on ACCESS-S1 hindcasts from 1990 to 2012 (without de-trending), is displayed in Fig. 8a. There is little skill in predicting the IOD for start dates prior to June, and the highest skill at long lead times is for the August to October start dates. The forecast performance of ACCESS-S1 for the IOD is similar to other coupled model seasonal prediction systems (Zhao and Hendon 2009; Shi et al. 2012). However, even from September and October start dates, the forecast skill drops off for austral summer months because the IOD rapidly decays in December. Consistent with the lack of hindcast skill to predict the spring-time IOD prior to July start times, the predicted DMI index for September 2019 did not display realistically large amplitude until forecasts initialized on 1 July (Fig. 8c).

In contrast to the IOD, CP El Niño/La Niña can be skilfully predicted by ACCESS-S1, based on correlation of observed and predicted EMI, for start times all year round (Fig. 8b). The long lead skill reflects the long persistence of the EMI (Hendon et al. 2009; Kug et al. 2009). However, the highest long lead skill for the EMI is for start times after May, which is after the so-called "northern spring

predictability barrier". Although positive EMI anomalies are predicted from as early as 1 April 2019, the predicted anomalies are consistently weaker than observed (Fig. 8c).

In light of the capability to predict both IOD and CP El Niño at least for short lead times from late winter and spring, we further assess the capability of ACCESS-S1 to predict  $T_{\min}$  extremes (bottom quintile) across Australia by computing the Receiver Operating Characteristic (ROC; also called the relative operating characteristic; Wilks 2006) curve using the hindcasts for 1990–2012 over all grid points of Australia (Fig. 9a, b) and the area under the ROC curve at each grid point (Fig. 9c, d) at zero (forecasts initialised on 1 September) and one month (forecasts initialised on 1 August) lead times. The ROC is computed as the ratio of the hit rate<sup>7</sup> versus false alarm rate<sup>8</sup> for predicting  $T_{\min}$  in the lowest quintile. The ROC is computed in ten equally sized probability thresholds from 0 to 1. In Fig. 9a, b, the curve above the no skill line indicates good forecast performance as it indicates greater hit rates than false alarm rates no matter what are the probability thresholds to issue an alarm for an event occurrence. For the area under the ROC curve, values greater than 0.5 are skilful relative to a random forecast, and a value of 1 is perfect.

ACCESS-S1 23-year hindcasts demonstrate overall high skill to predict low  $T_{\min}$  for September at both lead times, and the significantly high skill across much of eastern and northern Australia at zero lead time (Fig. 9a, c) is where the observed low values of  $T_{\min}$  occurred during 2019 (Fig. 2a). Although the skill declines at lead time of 1 month (Fig. 9b, d), skill remains high in the central east and north, suggesting that the anomalies during 2019 might have been well predicted. However, the forecast for September 2019 (Fig. 10a, b) failed to capture the extreme low  $T_{\min}$  across the east at lead time 0 and across the east and the north at lead time 1 month. These forecast busts imply a missed opportunity to forewarn the increased chance of the lower-than-normal minimum temperatures and frost formation in southern New South Wales, Victoria and eastern South Australia during September 2019. This forecast error appears to be related to the complete miss of the teleconnection of the positive IOD to locate a high pressure anomaly over the Bight (Fig. 10e, f) that drives northward and westward winds advecting the cold air over eastern Australia. Why did these forecast errors happen?

The capability of ACCESS-S1 to capture teleconnections from the IOD and CP El Niño is assessed by examining

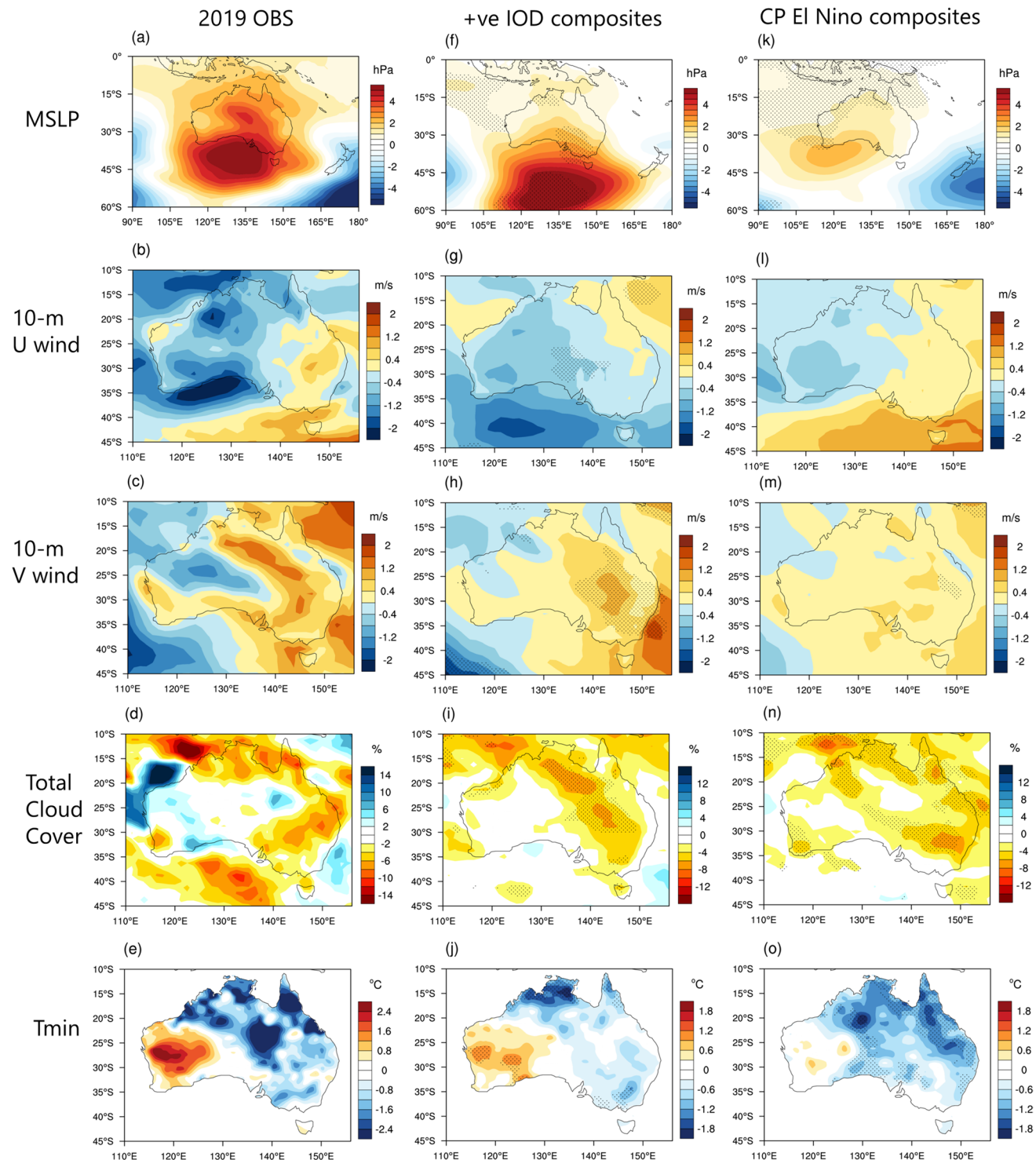
composite patterns of MSLP, 10-m horizontal winds, outgoing longwave radiation flux (used as a proxy for total cloud cover fraction) and  $T_{\min}$  during September for the strong positive IOD years and strong positive CP El Niño (not including 2019) using forecast data at zero lead time (Fig. 11). For the IOD, the predicted patterns have an overall resemblance to the observed composite patterns shown in Fig. 7 (middle column and also Supplementary Fig S5 for the same composite years), but the magnitudes of the anomalies are significantly smaller than the observed even at this shortest lead time. The forecast composite patterns for MSLP and horizontal winds for CP El Niño (Fig. 11f–h) show a hint of simulating the high pressure center southwest of Australia and associated circulation, but again the forecast anomalies are also not significantly different from the forecast mean conditions, highlighting that the teleconnections of the positive IOD and CP El Niño to Australian  $T_{\min}$  are substantially underpredicted in ACCESS-S1. The forecast outgoing longwave radiation anomalies during the positive IOD and CP El Niño years demonstrate unrealistic responses over Western Australia and a lack of sensitivity in the northern end of Australia. Consequently, ACCESS-S1 falls short in predicting lower-than-normal  $T_{\min}$  in September during positive IOD over south-eastern Australia and during CP El Niño over subtropical eastern Australia, where extreme low  $T_{\min}$  can have a significant impact on agriculture (Fig. 11e, j).

The inability of ACCESS-S1 to capture the impact of the positive IOD and CP El Niño on  $T_{\min}$  throughout a broad region of central and southern Australia is likely related to the systematic errors in simulation of the mean state of the tropical Indo-Pacific: the SST tends to be simulated to be too cold to the northwest of Australia, with too little rainfall, and stronger than observed south-easterly trade winds across the southern tropical Indian Ocean (Hudson et al. 2017). As the tropical Indian Ocean and western Pacific are where SST is high and associated convective rainfall is rich, the cold and dry mean state biases are translated into problems in simulating the teleconnection from the IOD to the extratropics (Hudson et al. 2017).

However, examination of the forecast for September 2019 (Fig. 10) also suggests that the model error for this particular case well exceeds the systematic errors in the depiction of the IOD and CP El Niño teleconnection that were discussed above. Closer inspection of the forecast surface pressure anomaly (Fig. 10e, f) reveals that the model was predicting strong low pressure anomalies south of Australia at both zero and 1 month lead times, which was likely related to a negative SAM forecast. The forecast at 1 month lead time for pressure anomalies in September 2019 simulated a

<sup>7</sup> The ratio of the correct forecasts for the occurrence of an event to the total number of forecasts.

<sup>8</sup> The ratio of the incorrect forecasts for the occurrence of an event (i.e., forecasts for the occurrence which are not observed) to the total number of forecasts.



strong negative SAM as judged by the forecast SAM index<sup>9</sup> being  $-1.3\sigma$ . The forecast at zero lead time still produced a

negative SAM for the month although it was weaker ( $-0.7\sigma$ ) (Supplementary Fig. S7). Negative SAM-dominant pressure forecasts were likely made for September 2019 as a result of the record-strong Antarctic polar stratospheric warming that developed from the last week of August 2019 (Lim et al. 2021; Rao et al. 2020). Consequently, clearer skies and increased downward compression of air over the Australian

<sup>9</sup> The SAM index in this study was obtained following Gong and Wang (1999)'s definition, which is the difference of normalised zonal-mean MSLP anomalies between  $40^{\circ}$  S and  $65^{\circ}$  S.

**Fig. 7** (Left column; **a–e**) September 2019 anomalies of **a** MSLP (hPa), **b** 10-m zonal wind ( $\text{m s}^{-1}$ ), **c** 10-m meridional wind ( $\text{m s}^{-1}$ ), **d** total cloud cover fraction (%), and **e**  $T_{\min}$  ( $^{\circ}\text{C}$ ). (Middle column; **f–j**) Respective composites of the same fields as in **a–e** for the five strongest positive IOD years in 1979–2018 (listed in Table 1). (Right column; **k–o**) Same as **f–j** but for the five strongest central Pacific El Niño years (listed in Table 1). Anomalies of total cloud cover fraction were computed relative to the climatological fraction. Composite anomalies displayed in the middle and right columns are de-trended to highlight the anomalies associated with the naturally driven IOD and CP El Niño events. Note that for **d**, **i**, **n** red colour shading indicates the reduction of the cloud cover and blue colour shading indicates the increase of the cloud cover. The colour contour scales are different between the observation and the composites for the 10-m meridional wind anomalies (**c**, **h**, **m**) and for the  $T_{\min}$  anomalies (**e**, **j**, **o**). Stippling in the middle and right columns indicates the statistical significance on the difference of the two means (composite mean vs. climatological mean) at the 10% level, assessed by the two-tailed Student *t* test with the samples sizes of five in the composite groups of the strong positive IOD and the strong central Pacific El Niño, respectively, and 23 in the climatological group

continent, which are known as the responses to the negative SAM (Lim et al. 2019), were predicted (Figs. 10c,d,g,h), resulting in high  $T_{\min}$  being adiabatically promoted in the model. However, in reality the stratospheric warming did not couple down to the surface until the 3rd week of October, and so the SAM was actually positive in September as indicated by the observed SAM index being  $+0.6\sigma$  (Lim et al. 2021). Furthermore, a pronounced high pressure anomaly associated with the positive IOD was dominant over the Bight during September as shown in Fig. 7a and Supplementary Fig. 7a.

We thus speculate that ACCESS-S1 was prematurely predicting negative SAM during September in response to the stratospheric warming partly because of the too-weak teleconnection from the IOD and CP El Niño. Rao et al. (2020) demonstrated that the same error of predicting negative September SAM in 2019 was found in the multi-model mean prediction consisting of the five different major international centre models. In general, dynamical seasonal forecast systems including ACCESS-S1 show reasonably high skill to predict the SH stratospheric spring-time polar vortex variability and its linkage to the tropospheric SAM when forecasts are initialised at the beginning of August (e.g., Seviour et al. 2014; Hendon et al. 2020; Lim et al. 2020, 2021), and they skilfully predicted the rare extreme stratospheric warming event of 2019 from late July 2019 (Lim et al. 2021; Rao et al. 2020). Thus, further work is required to better understand the source of this common error of prematurely predicting negative SAM across the forecast systems.

To further gain insight into the apparently high skill for predicting  $T_{\min}$  across much of the east based on the hindcasts but the failure during 2019, we also assess the capability of ACCESS-S1 to depict the  $T_{\min}$  anomalies associated with the negative IOD and CP La Niña (compare

Supplementary Fig. S8 to Figs. S4 and S6). For these cases, the model performs much better in capturing the higher-than-normal  $T_{\min}$  over the north and subtropical east of Australia predominantly caused by the reduced outgoing longwave radiation representing higher cloud cover as observed. Therefore, the forecast skill for September  $T_{\min}$  across much of the east and north as shown in Fig. 9, seems to reflect the forecast skill in predicting  $T_{\min}$  during negative IODs and CP La Niñas.

### 3 Concluding remarks

Northern and eastern Australia experienced very unusual low minimum temperatures during September 2019, which were recorded to be in the bottom two deciles (i.e., bottom quintile) based on the past 40 year record. The number of days with minimum temperatures below  $2^{\circ}\text{C}$  and  $0^{\circ}\text{C}$ , which are indicators of potential frost damage, was significantly larger along and north of the Dividing Range in Victoria, South Australia and southern New South Wales, indicating a potential increase of frost formation. We have shown that, historically, reduced September-mean  $T_{\min}$  across northern and eastern Australia is related to the occurrence of the positive IOD and CP El Niño, which are monitored by the DMI and the EMI, respectively. The teleconnection of the positive IOD to the Southern Hemisphere extratropics is characterised by a well-defined high pressure anomaly over the Great Australian Bight (e.g., Cai et al. 2011; McIntosh and Hendon 2018), which promotes cold air advection from the south to eastern Australia. Furthermore, for both positive IOD and CP El Niño, reduced cloud cover in the northern and eastern portions of Australia is associated with lower  $T_{\min}$ , allowing more outgoing longwave radiation at night.

In September 2019 the IOD was the 2nd strongest positive and central Pacific El Niño was the 3rd strongest for the month in the past 40-year record of Reynolds OI version 2 SST data (Reynolds et al. 2002) appended to Hurrell et al. (2008) SST data. The observed 2019 September  $T_{\min}$  anomalies are well reconstructed using regressions onto the de-trended DMI and EMI during the period 1979–2018, then scaling the coefficients by the amplitudes of the de-trended DMI and EMI in September 2019. This reconstruction suggests that the September 2019  $T_{\min}$  anomalies should be well predicted because September IOD is skilfully predictable at least with 2 month lead time and September central Pacific El Niño is skilfully predictable at beyond 2 season lead time using the ACCESS-S1 system. However, even at zero lead time, ACCESS-S1 failed to predict the cold conditions over eastern Australia of September 2019 largely because of its failure to predict the anomalous high in the Bight that is predominantly

**Table 1** The five strongest positive and negative IOD and central Pacific El Niño years based on September-mean values of the de-trended DMI and the de-trended EMI

	Positive	Negative
DMI	<b>1994</b>	<b>1992</b>
	<b>1997</b>	<b>1998</b>
	<b>2006</b>	<b>2005</b>
	<b>2007</b>	<b>2010</b>
	2015	2016
EMI	<b>1990</b>	1983
	<b>1991</b>	1988
	<b>1994</b>	<b>1998</b>
	<b>2002</b>	<b>2008</b>
	<b>2004</b>	<b>2010</b>

Bold-faced numbers indicate the years when the ACCESS-S1 hindcasts are available

associated with the positive IOD and, to a lesser extent, with central Pacific El Niño.

Analysis of the ACCESS-S1 hindcasts indicates that the simulated IOD and central Pacific El Niño teleconnections are systematically too weak to drive the  $T_{\min}$  variability in eastern Australia and especially in the south, which leads to forecast busts for the  $T_{\min}$  in September when cold extreme forecasts can be very important and useful over south-eastern Australia. This weak teleconnection may have contributed to the incorrect early expression of negative SAM following the sudden stratospheric warming that occurred in late August 2019. The cause of the too weak IOD teleconnection is the focus of on-going work, but presumably reflects in part the strong systematic biases in the mean state of the tropical Indian Ocean (e.g., Hudson et al. 2017) that are key to faithful depiction of the IOD.

Although it was not a topic of the current research, Risbey et al (2019) show that extreme frost events typically occur at the leading edge of a blocking high, and there were two short-lived split-flow blocking events, peaking on September 6 and September 22–23 in 2019, which also could have contributed to the night-time cold extreme. Understanding these short lived blocking events and their interactions with the anomalous large-scale drivers and the Australian cold extreme episode of September 2019 will be worth exploring in a separate study.

The extreme  $T_{\min}$  that occurred in September 2019 coincided with both drought and extreme high day-time temperatures over much of south-eastern and eastern Australia, driven by the strongly positive IOD and central Pacific El Niño. This is a critical time of year for many agricultural sectors in Australia that are sensitive to any one of these

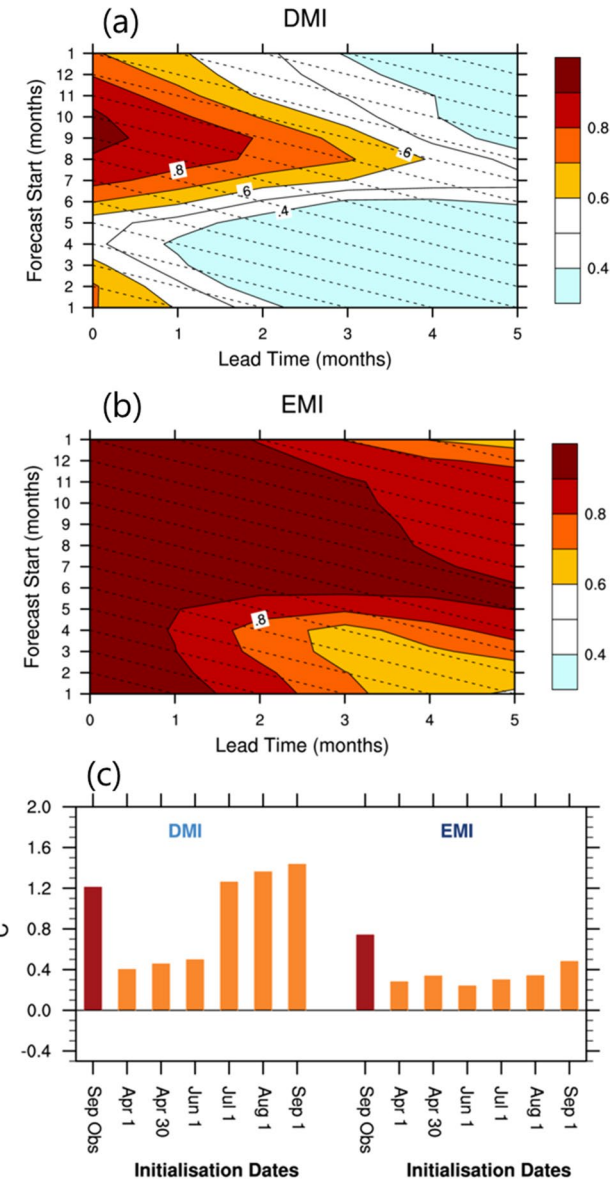


**Fig. 8** **a** ACCESS-S1 hindcast skill to predict the DMI as a function of forecast start month (y axis) and lead time (x axis). **b** Same as **a** except for the EMI. **c** Forecasts for DMI and EMI September 2019 from different start times (orange colour bars). The red colour bars in **c** are the observed amplitudes of the DMI and the EMI in September 2019

local climate extremes, and so exposure to all three simultaneously places significant stress on the industry. Therefore, understanding the drivers of these conditions and the pathways to improved prediction skill of  $T_{\min}$  in association with IOD and CP El Niño should be a high priority of research.

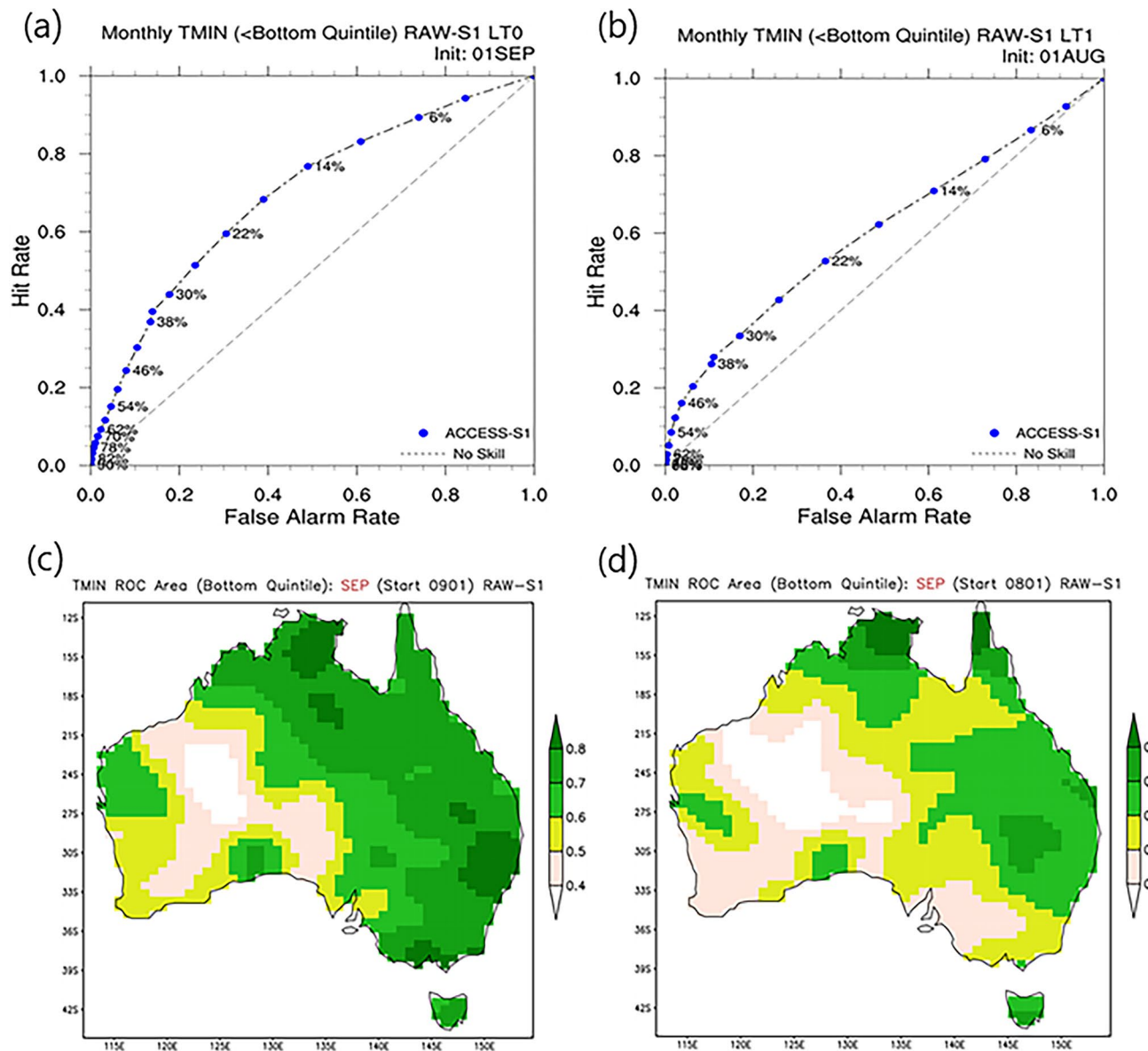


**Fig. 9** **a, b** ROC curves for forecasts of bottom quintile  $T_{\min}$  for September displayed as a function of hit rates versus false alarm rates using all the land points over Australia in the hindcast period 1990–2012 at lead times of 0 and 1 month, respectively. The blue dots indicate the forecast probability thresholds to define the forecast occur-

rence for an event. The diagonal line indicates no skill. **c, d** Forecast skill measured by the area under the ROC curve for predicting bottom quintile  $T_{\min}$  for September at lead time 0 and 1 month at each grid point

**Fig. 10** Forecasts from ACCESS-S1 for **a, b**  $T_{\min}$  ( $^{\circ}\text{C}$ ), **c, d** outgoing longwave radiation flux ( $\text{W m}^{-2}$ ), **e, f** MSLP (hPa), and **g, h** 500 hPa geopotential height (m) anomalies for September 2019 at 0 and 1 month lead times

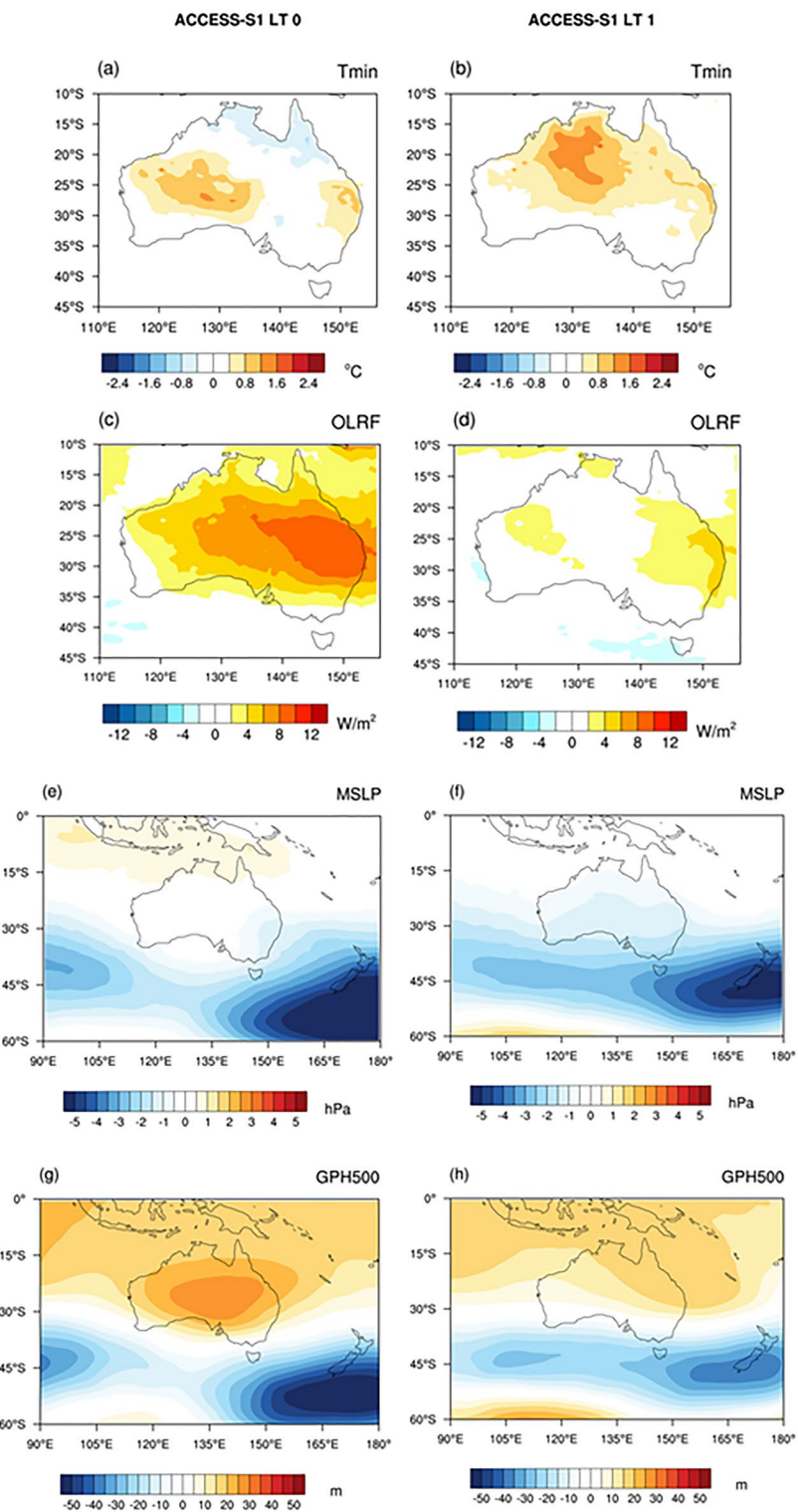
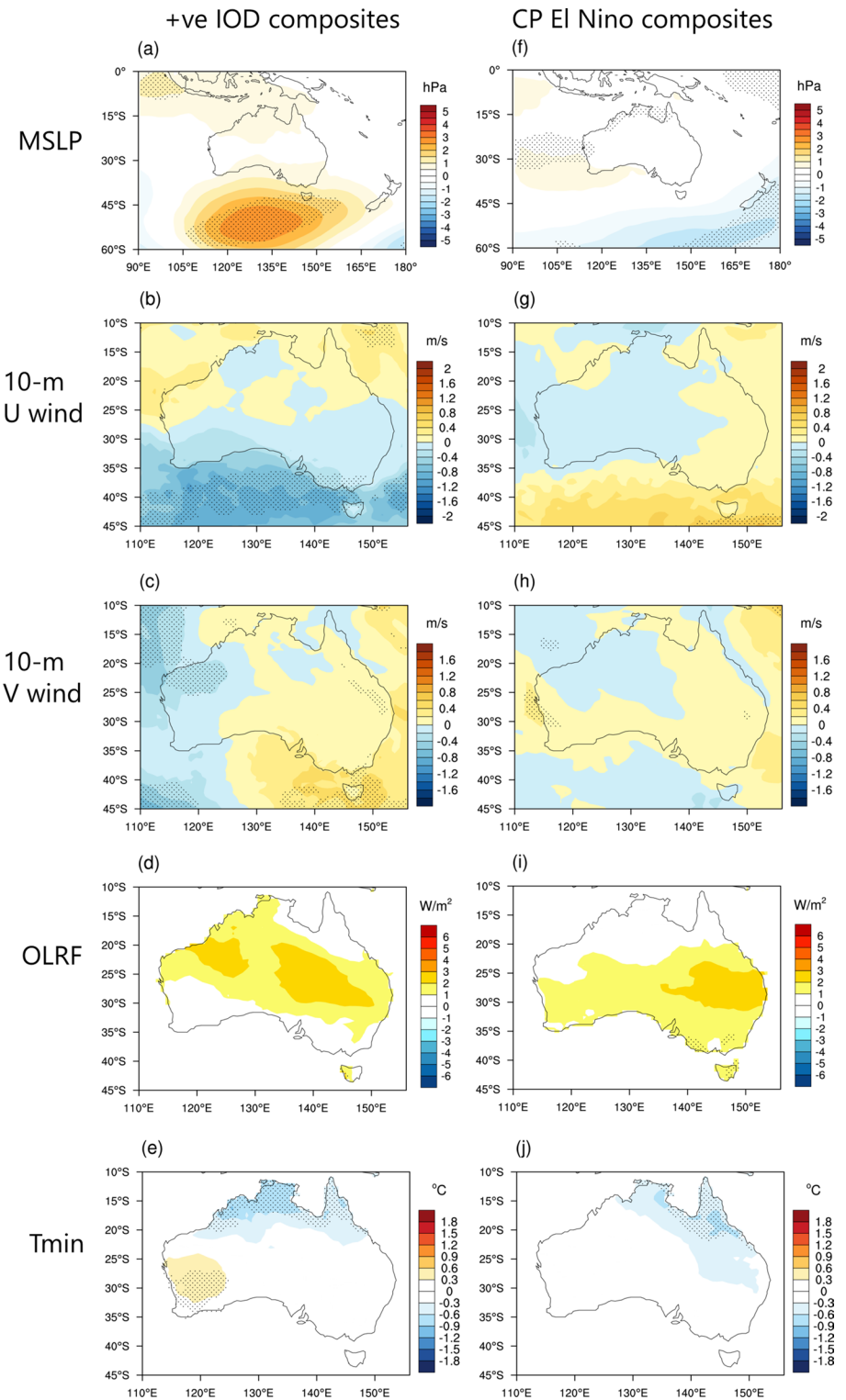


**Fig. 11** Composites of ensemble mean forecast anomalies at lead time zero for **a, f** MSLP (hPa), **b, g** 10-m zonal wind ( $\text{m s}^{-1}$ ), **c, h** 10-m meridional wind ( $\text{m s}^{-1}$ ), **d, i** outgoing longwave radiation flux ( $\text{W m}^{-2}$ ), and **e, j**  $T_{\min}$  ( $^{\circ}\text{C}$ ) during the four strongest positive IOD years (left column) and the five strongest central Pacific El Niño years (right column). The years for each category are listed in Table 1 (but only the years within the hindcast period of 1990–2012). Stippling indicates the statistical significance on the difference of the two means at the 10% level, assessed by a Student t test with the sample sizes of four and five in the IOD and CP El Niño composite groups, respectively, and 23 in the climatological group



**Supplementary Information** The online version contains supplementary material available at <https://doi.org/10.1007/s00382-021-05661-8>.

**Acknowledgements** This project is supported by funding from the Australian Government Department of Agriculture and Water Resources as part of its Rural R&D for Profit programme. Andrew King was supported by the Australian Research Council (DE180100638). We are grateful to Dr Alex Pezza and an anonymous reviewer for their thorough review and constructive feedback on the manuscript and to Professor Jianping Li for his editorial effort to coordinate the peer-review process. We thank Dr Peter Hayman at SARDI and Mr Dale Grey at Agriculture Victoria for the useful discussion on the subject of this study and Drs Sharmila Sur and Guomin Wang at the BoM for their constructive feedback on the initial version of the manuscript. We also thank Dr Robin Wedd, Mr Griffith Young and other members of the seasonal prediction teams at the BoM for their work in the generation and curation of the ACCESS-S1 hindcast set. This research was undertaken on the NCI National Facility in Canberra, Australia, which is supported by the Australian Commonwealth Government. The NCAR Command Language (NCL; <http://www.ncl.ucar.edu>) version 6.4.0 and IDL version 8.7.3 were used for data analysis and visualization of the results. We also acknowledge NCAR/UCAR and JMA for producing and providing the Hurrell et al. (2008) SST analysis and the JRA-55 reanalyses, respectively.

**Funding** Support was provided from the Australian Government Department of Agriculture and Water Resources as part of its Rural R&D for Profit programme. Andrew King was supported by the Australian Research Council (DE180100638).

**Availability of data and material** The JRA-55 reanalyses are available from <https://rda.ucar.edu/>. The Hurrell SST analyses are available from: <https://climatedataguide.ucar.edu/climate-data/merged-hadley-noaa-ocean-surface-temperature-sea-ice-concentration-hurrell-et-al-2008>. The AWAP Australian temperature and rainfall analyses are available from the Australian Bureau of Meteorology: "Australian Gridded Climate Data (AGCD)/AWAP; v1.0.0 Snapshot (1900-01-01 to 2018-12-31)" (<https://doi.org/10.4227/166/5a8647d1c23e0>). The ACCESS-S1 hindcasts and real time prediction system are described in Hudson et al. (2017).

**Code availability** The NCAR Command Language (NCL; <http://www.ncl.ucar.edu>) version 6.4.0 and IDL version 8.7.3 were used for data analysis and visualization of the results.

## Compliance with ethical standards

**Conflict of interest** The authors declare that they have no conflict of interest.

## References

- Ashok K, Behera SK, Rao SA et al (2007) El Niño Modoki and its possible teleconnection. *J Geophys Res Ocean* 112(C11007). <https://doi.org/10.1029/2006JC003798>
- Bange MP, Milroy SP (2004) Impact of short-term exposure to cold night temperatures on early development of cotton (*Gossypium hirsutum* L.). *Aust J Agric Res* 55:655–664
- Boer MM, Resco de Dios V, Bradstock RA (2020) Unprecedented burn area of Australian mega forest fires. *Nat Climate Chang* 10:171–172. <https://doi.org/10.1038/s41558-020-0710-7>
- Cai W, van Renssch P, Cowan T, Hendon HH (2011) Teleconnection pathways of ENSO and the IOD and the mechanisms for impacts on Australian rainfall. *J Climate* 24:3910–3923. <https://doi.org/10.1175/2011JCLI4129.1>
- Cowan T, Wheeler MC, Alves O et al (2019) Forecasting the extreme rainfall, low temperatures, and strong winds associated with the northern Queensland floods of February 2019. *Weather Climate Extrem* 26:100232
- Crimp SJ, Gobbett D, Kokic P et al (2016) Recent seasonal and long-term changes in southern Australian frost occurrence. *Clim Change* 139:115–128. <https://doi.org/10.1007/s10584-016-1763-5>
- Dee D, Uppala S, Simmons A et al (2011) The ERA—interim reanalysis: configuration and performance of the data assimilation system. *Q J R Meteorol Soc* 137:553–597. <https://doi.org/10.1002/qj.828>
- Dittus AJ, Karoly DJ, Lewis SC, Alexander LV (2014) An investigation of some unexpected frost day increases in southern Australia. *Aust Meteorol Ocean J* 64:261–271
- Frederiks TM, Christopher JT, Sutherland MW, Borrell AK (2015) Post-head-emergence frost in wheat and barley: defining the problem, assessing the damage, and identifying resistance. *J Exp Bot* 66:3487–3498. <https://doi.org/10.1093/jxb/erv088>
- Gong D, Wang S (1999) Definition of Antarctic Oscillation index. *Geophys Res Lett* 26:459–462. <https://doi.org/10.1029/1999GL900003>
- Grantz DA (1989) Effect of cool temperatures on photosynthesis and stomatal conductance in field-grown sugarcane in Hawaii. *F Crop Res* 22:143–155
- Grose MR, Black M, Risbey JS et al (2018) Severe frosts in Western Australia in September 2016. *Bull Am Meteorol Soc* 99:S150–S154. <https://doi.org/10.1175/BAMS-D-17-0088.1>
- Hatfield JL, Prueger JH (2015) Temperature extremes: effect on plant growth and development. *Weather Climate Extrem* 10:4–10. <https://doi.org/10.1016/j.wace.2015.08.001>
- Hendon HH, Thompson DWJ, Wheeler MC (2007) Australian rainfall and surface temperature variations associated with the Southern Hemisphere Annular Mode. *J Climate* 20:2452–2467. <https://doi.org/10.1175/JCLI4134.1>
- Hendon HH, Lim E, Wang G et al (2009) Prospects for predicting two flavors of El Niño. *Geophys Res Lett* 36(L19713). <https://doi.org/10.1029/2009GL040100>
- Hendon HH, Lim E-P, Liu G (2012) The role of air-sea interaction for prediction of Australian summer monsoon rainfall. *J Climate* 25:1278–1290. <https://doi.org/10.1175/JCLI-D-11-00125.1>
- Hendon HH, Lim E-P, Abhik S (2020) Impact of interannual ozone variations on the downward coupling of the 2002 southern hemisphere stratospheric warming. *J Geophys Res Atmos* 125(e2020JD032952). <https://doi.org/10.1029/2020JD032952>
- Hudson D et al (2017) ACCESS-S1 The new Bureau of Meteorology multi-week to seasonal prediction system. *J S Hemisph Earth Syst Sci* 67:132–159. <https://doi.org/10.22499/3.6703.001>
- Hurrell JW, Hack JJ, Shea D et al (2008) A new sea surface temperature and sea ice boundary dataset for the community atmosphere model. *J Climate* 21:5145–5153. <https://doi.org/10.1175/2008JCLI2292.1>
- Jacobs BC, Pearson CJ (1999) Growth, development and yield of rice in response to cold temperature. *J Agron Crop Sci* 182:79–88
- Jones D, Wang W, Fawcett R (2009) High-quality spatial climate data-sets for Australia. *Aust Meteorol Oceanogr J* 58:233–248
- Kalma JD, Laughlin GP, Caprio JM, Hamer PJC (1992) The occurrence of frost: types, distribution and prediction. In: The bioclimatology of frost. Advances in bioclimatology, vol 2. Springer, Berlin

- Kao HY, Yu JY (2009) Contrasting Eastern-Pacific and Central-Pacific types of ENSO. *J Clim* 22:615–632. <https://doi.org/10.1175/2008JCLI2309.1>
- Keller M, Tarara JM, Mills LJ (2010) Spring temperatures alter reproductive development in grapevines. *Aust J Grape Wine Res* 16:445–454
- Kobayashi S, Ota Y, Harada Y et al (2015) The JRA-55 reanalysis: general specifications and basic characteristics. *J Meteorol Soc Japan Ser II* 93:5–48. <https://doi.org/10.2151/jmsj.2015-001>
- Kug J-S, Jin F-F, An S-I (2009) Two types of El Niño events: cold tongue El Niño and Warm Pool El Niño. *J Clim* 22:1499–1515. <https://doi.org/10.1175/2008JCLI2624.1>
- Lim E, Hendon HH (2015) Understanding the contrast of Australian springtime rainfall of 1997 and 2002 in the frame of two flavors of El Niño. *J Climate* 28:2804–2822. <https://doi.org/10.1175/JCLI-D-14-00582.1>
- Lim E, Hendon HH, Boschat G et al (2019) Australian hot and dry extremes induced by weakenings of the stratospheric polar vortex. *Nat Geosci* 12:896–901. <https://doi.org/10.1038/s41561-019-0456-x>
- Lim E, Hendon HH, Butler AH et al (2020) The 2019 Antarctic sudden stratospheric warming. *SPARC News* 54:10–13
- Lim E, Hendon HH, Butler AH et al (2021) The 2019 Southern Hemisphere stratospheric polar vortex weakening and its impacts. *Bull Am Meteorol Soc*. <https://doi.org/10.1175/BAMS-D-20-0112.1>
- MacLachlan C, Arribas A, Peterson KA et al (2015) Global seasonal forecast system version 5 (GloSea5): a high-resolution seasonal forecast system. *Q J R Meteorol Soc* 141:1072–1084. <https://doi.org/10.1002/qj.2396>
- Marshall AG, Hudson D, Wheeler MC et al (2014) Intra-seasonal drivers of extreme heat over Australia in observations and POAMA-2. *Climate Dyn* 43:1915–1937. <https://doi.org/10.1007/s00382-013-2016-1>
- McIntosh PC, Hendon HH (2018) Understanding Rossby wave trains forced by the Indian Ocean Dipole. *Clim Dyn* 50:2783–2798. <https://doi.org/10.1007/s00382-017-3771-1>
- Pook MJ, Lisson S, Risbey J et al (2009) The autumn break for cropping in southeast Australia: trends, synoptic influences, and impacts on wheat yield. *Int J Clim* 29:2012–2026
- Rao J, Garfinkel CI, White IP, Schwartz C (2020) The southern hemisphere sudden stratospheric warming in September 2019 and its predictions in S2S Models. *J Geophys Res Atmos* 125(e2020JD032723). <https://doi.org/10.1029/2020JD032723>
- Rayner NAA, Parker DE, Horton EB, Folland CK, Alexander LV, Rowell DP, Kent EC, Kaplan A (2003) Global analyses of sea surface temperature, sea ice, and night marine air temperature since the late nineteenth century. *J Geophys Res Atmos* 108 (D14)
- Rebbeck M, Lynch C, Hayman PT, Sadras V (2007) Delving of sandy surfaced soils reduces frost damage in wheat crops. *Aust J Agric Res* 58:1–8
- Reynolds RW, Rayner NA, Smith TM et al (2002) An improved in situ and satellite SST analysis for climate. *J Climate* 15:1609–1625. [https://doi.org/10.1175/1520-0442\(2002\)015%3c1609:AIISA%3e2.0.CO;2](https://doi.org/10.1175/1520-0442(2002)015%3c1609:AIISA%3e2.0.CO;2)
- Risbey JS, Pook MJ, McIntosh PC et al (2009) On the remote drivers of rainfall variability in Australia. *Mon Weather Rev* 137:3233–3253. <https://doi.org/10.1175/2009MWR2861.1>
- Risbey JS, Monselesan DP, O’Kane TJ et al (2019) Synoptic and large-scale determinants of extreme austral frost events. *J Appl Meteorol Climatol* 58:1103–1124. <https://doi.org/10.1175/JAMC-D-18-0141.1>
- Saji NH, Goswami BN, Vinayachandran PN, Yamagata T (1999) A dipole mode in the tropical Indian Ocean. *Nature* 401:360–363. <https://doi.org/10.1038/43854>
- Saji NH, Ambrizzi T, Ferraz SET (2005) Indian Ocean Dipole mode events and austral surface air temperature anomalies. *Dyn Atmos Ocean* 39:87–101. <https://doi.org/10.1016/j.dynatmoc.2004.10.015>
- Seviour WJM, Hardiman SC, Gray LJ et al (2014) Skillful seasonal prediction of the Southern Annular Mode and Antarctic ozone. *J Climate* 27:7462–7474. <https://doi.org/10.1175/JCLI-D-14-00264.1>
- Shi L, Hendon HH, Alves O et al (2012) How predictable is the Indian Ocean dipole? *Mon Weather Rev* 140:3867–3884. <https://doi.org/10.1175/MWR-D-12-00001.1>
- Thompson DWJ, Wallace JM (2000) Annular Mode in the extratropical circulation. Part I: month-to-month variability. *J Clim* 13:1000–1016. [https://doi.org/10.1175/1520-0442\(2000\)013%3c1000:AMITEC%3e2.0.CO;2](https://doi.org/10.1175/1520-0442(2000)013%3c1000:AMITEC%3e2.0.CO;2)
- Trewin B (2018) The Australian climate observations reference network – surface air temperature (ACORN-SAT) version 2. Bureau Research Report No. 32, Bureau of Meteorology, Australia. <http://www.bom.gov.au/research/publications/researchreports/BRR-032.pdf>
- Trewin B, Braganza K, Fawcett R et al (2020) An updated long-term homogenized daily temperature data set for Australia. *Geosci Data J.* <https://doi.org/10.1002/gdj3.95>
- Ummenhofer CC, England MH, McIntosh PC et al (2009) What causes southeast Australia’s worst droughts? *Geophys Res Lett* 36(L04706). <https://doi.org/10.1029/2008GL036801>
- Wang G, Hendon HH (2007) Sensitivity of Australian rainfall to inter-El Niño variations. *J Climate* 20:4211–4226. <https://doi.org/10.1175/JCLI4228.1>
- Waters J, Lea DJ, Martin MJ, Miroze I, Weaver A, While (2015) Implementing a variational data assimilation system in an operational 1/4 degree global ocean model. *Q J Roy Meteorol Soc* 141:333–349. <https://doi.org/10.1002/qj.2388>
- Webster JR, Stewart M, Rogers AR, Verkerk GA (2008) Assessment of welfare from physiological and behavioural responses of New Zealand dairy cows exposed to cold and wet conditions. *Anim Welf* 17:19–26
- Wilks DS (2006) Statistical methods in the atmospheric sciences, 2nd edn. Academic Press Inc, New York
- Zhang X, Alexander L, Hegerl GC et al (2011) Indices for monitoring changes in extremes based on daily temperature and precipitation data. *WIREs Climate Chang* 2:851–870
- Zhao M, Hendon HH (2009) Representation and prediction of the Indian Ocean Dipole in the POAMA seasonal forecast model. *Q J R Meteorol Soc* 135:337–352. <https://doi.org/10.1002/qj.370>
- Zheng B, Chapman SC, Christopher JT et al (2015) Frost trends and their estimated impact on yield in the Australian wheatbelt. *J Exp Bot* 66:3611–3623. <https://doi.org/10.1093/jxb/erv163>

**Publisher's Note** Springer Nature remains neutral with regard to jurisdictional claims in published maps and institutional affiliations.